# Experimental evaluation of phase-field-based load-specific shape optimization of nature-inspired porous structures

Leonie Wallat [b,c,*], Arnd Koeppe [c,d], Michael Selzer [b,d], Marcus Seiler [e], Frank Poehler [b], Britta Nestler [a,c,d]

[a] Institute of Digital Materials Science, Karlsruhe University of Applied Sciences, Moltkestraße 30, 76133 Karlsruhe, Germany
[b] Institute of Materials and Processes, Karlsruhe University of Applied Sciences, Moltkestraße 30, 76133 Karlsruhe, Germany
[c] Institute for Applied Materials - Microstructure Modelling and Simulation, Karlsruhe Institute of Technology (KIT), Strasse am Forum 7, 76131 Karlsruhe, Germany
[d] Institute of Nanotechnology, Karlsruhe Institute of Technology (KIT), Hermann-von-Helmholtz-Platz 1, 76344 Eggenstein-Leopoldshafen, Germany
[e] ReOss GmbH, Echterdinger Str. 57, 70794 Filderstadt, Germany

*Keywords:*
TPMS structures
Phase-field method
Shape optimization
Experimental validation

A B S T R A C T

Triply periodic minimal surface (TPMS) structures excel in various research fields, ranging from bone support structures to heat exchangers. By implementing measures for shape alteration, the mechanical properties of the structure can be improved under certain load conditions. While interface-based methods such as the phase-field method have established themselves as powerful simulation techniques for the analysis of microstructure evolution and morphologically complex dynamic processes, they are not yet very well known and widely used for the application of shape optimization in mechanically loaded complex structures. In this study, an experimental procedure to validate shape-optimized samples is presented and applied to validate three computationally derived optimal candidates for sheet-based TPMS structures (Diamond, Gyroid, and Primitive) proposed by applying a mathematical model for shape optimization formulated in terms of the phase-field approach combined with linear elastic continuum mechanics and subject to the constraints of volume conservation. The present experimental study aims to validate recently obtained theoretical research results predict three different TPMS structures were shape-optimized under mechanical stress, using the phase-field method. In the following, the previous theoretical study is validated experimentally. The validation procedure creates a rare intersection between shape optimization phase-field simulations and experimental samples. The measurements show that the shape-optimized structures have a higher average stiffness, which leads to a shift in the plastic deformation range and thus confirms the computationally determined shape optimization.

## 1. Introduction

Nature-inspired structures are widely considered designs in research and application [1,2]. Cellular structures are an example particularly indispensable for lightweight construction [2]. These structures are often characterized by their high rigidity and low weight [3]. The possibility of computer-aided simulations now makes it possible to develop new, load-appropriate geometries and materials. In this context, the application-specific optimization of porous structures represents a promising domain. Particularly in tissue engineering, cellular structures are employed as bone implants to facilitate bone growth in the corresponding damaged regions. Optimal mechanical properties, which align with those of the implantation site, are crucial. For example, high porosity is essential to support adequate nutrient transport and cell growth [4]. Furthermore, investigations have shown that the effective Young modulus plays a crucial role in regulating bone growth [5]. A promising structure for stimulating bone growth is inspired by natural structures from the triply periodic minimal surface (TPMS) family. TPMS structures are naturally occurring, mathematically generable structures characterized by a minimal surface area with zero mean curvature at any point [6]. The resulting smooth, curved surface with a high surface-to-volume ratio and high porosity provides favorable cell adhesion, migration, and proliferation for bone cells [7]. Thanks to the ongoing development of manufacturing techniques such as additive manufacturing or 3D printing, producing complex porous structures is often no longer a challenge [8,9]. Al-Ketan et al. [8] provide an overview of the many possible applications of TPMS-based lattice structures. In Fig. 1, the top three structures (a, b, c) represent different sheet-based TPMS unit cells (Diamond, Gyroid, and Primitive).

* Corresponding author at: Institute of Materials and Processes, Karlsruhe University of Applied Sciences, Moltkestraße 30, 76133 Karlsruhe, Germany.
*E-mail address:* leonie.wallat@partner.kit.edu (L. Wallat).

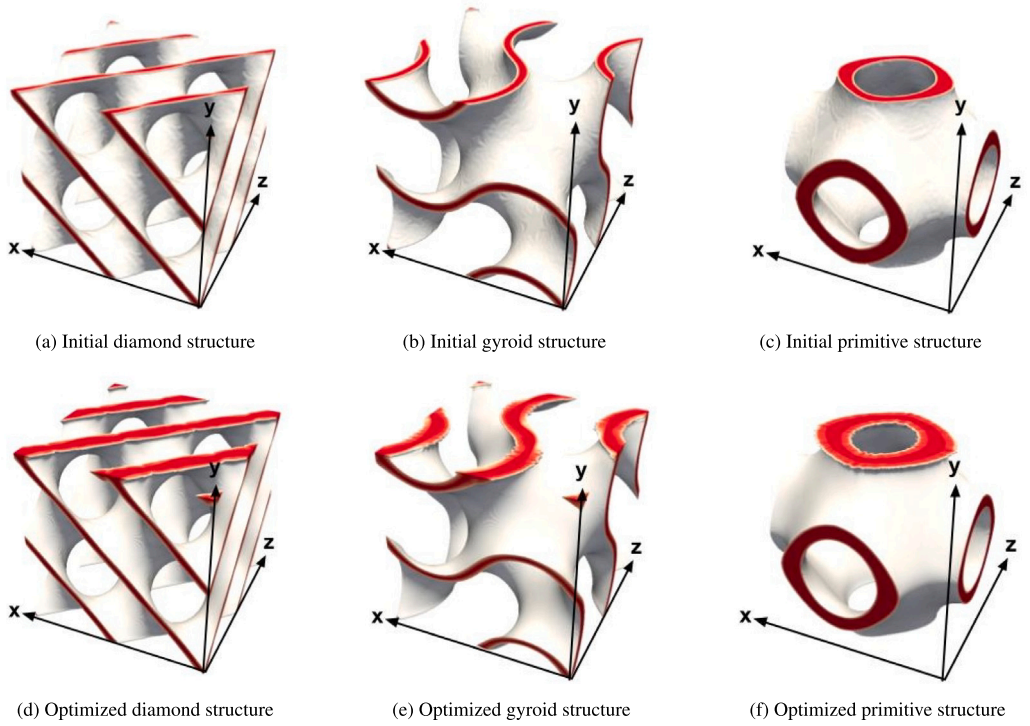


(a) Initial diamond structure (b) Initial gyroid structure (c) Initial primitive structure

(d) Optimized diamond structure (e) Optimized gyroid structure (f) Optimized primitive structure

**Fig. 1.** Unitcell sheet-based TPMS structures before (top) and after (bottom) shape optimization, based on diamond (a, d), gyroid (b, e), and primitive (c, f) structures.

To ensure both high porosity and high stiffness, TPMS structures have been shape-optimized in various studies. Since the simulation and optimization of complex structures remains a challenge, manual optimization approaches are often chosen, such as heuristically changing the porosity of the structure, the cell size or both, depending on the application or loading conditions [10–14]. For instance, in [12], a gradient was applied to the cell size in TPMS structures to replicate a lattice structure for bone. This manual shape optimization has been demonstrated to increase the stiffness. An alternative approach, rarely used for TPMS until now, involves the application of explicit optimization methods within a given domain of finite elements [15]. The application-specific optimization of microstructures leads to a material-independent structural improvement, which promises a significant impact on various areas of engineering. The motivation for the optimization varies depending on the application: For example, it may involve improving the thermal [16], flow-based [17,18] or mechanical [19,20] properties. Apart from the element-based methods, there are also methods based on boundary variation, for example the phase-field method. The phase-field method is a flexible simulation technique that provides accurate results for research problems such as fracture. In this field, the validation between experimental and simulation data has already been demonstrated in various studies. Pech et al. [21] showed agreement in simulations of fracture mechanics with wood. Similarly, [22] conducted an experimental investigation of phase separation with the theoretical phase-field model, using the Cahn-Hilliard equation. Pham [23] compared the analysis results of the phase-field model with experimental data and showed agreement between the model and the experimental observations. Although the phase-field method has already been validated experimentally in various fields, this validation is still largely missing in the field of shape and topology optimization [19,24,25]. In [19], it was shown that using the volume-conserving Allen-Cahn approach could reduce the high computational costs associated with the Cahn-Hilliard approach in structural topology optimization. This study aims to experimentally validate TPMS structures that have been shape-optimized for specific loads, using the phase-field method. To the best of the authors knowledge, such an investigation has not been conducted before. This work is a continuation of a previously published theoretical study [26], in which three different sheet-based triply periodic minimal surface unit cells (Diamond, Gyroid and Primitive) with a porosity of approximately 85 % were shape-optimized under mechanical compressive loading, using a recently formulated phase-field method based on the volume-preserving Allen-Cahn model, combined with objectify functions for algorithmically computed shape optimization. At 14.8 %, the single-cell diamond structure had the highest volume fraction of the three structures considered, followed by the gyroid structure with 14.6 % and the primitive structure with 14.3 %. For the simulation, the material properties of an isotropic material with a mass density of 2680 $kg/mm^3$, a Young modulus of 59 GPa, and a Poisson ratio of 0.35 were homogenized. Homogenization enables the results to be transferred from the micro to the macro level. Accordingly, the corresponding analysis values, such as the effective Young modulus, were converted to dimensionless values. The driving force of the phase-field method is coupled to the elastic strain energy, using the Allen-Cahn approach. In addition, volume preservation improved comparability with the optimized structures. To preserve the original shape of the TPMS structures, the simulation was terminated as soon as the topology of the initial structure changed. Moreover, the periodicity of the structures in the x- and $z$-directions was maintained. In the first row, Fig. 1 shows the initial TPMS structures for the individual unit cells. For application-specific shape optimization, the structures were unidirectionally subjected to a constant compressive load of 400 MPa in the $y$-direction. During the shape optimization process, material redistribution occurred. Material is added adjacent to heavily stressed areas and removed in less stressed areas. As a result, a volume shift is observed in the upper region of the shape-optimized structures, where the structure is subjected to a compressive load in the $y$-direction. The resulting unit cells are shown in the second row of Fig. 1.

While the initial structure was retained, the periodicity in the $y$-direction was interrupted by the load-specific shape optimization. Table 1 shows that the method maintains the approximate solids volume of 15 %, while increasing the surface-to-volume ratio during shape optimization for the primitive structure, compared to the original structure. For the diamond and gyroid structures, the surface-to-volume ratio remains constant throughout the optimization process. This aspect is

**Table 1**
Structural and mechanical properties of the initial and shape-optimized structures.

| Structure: | Diamond | | | Gyroid | | | Primitive | | |
|---|---|---|---|---|---|---|---|---|---|
| | Volume fraction | Surface/ volume ratio | Young's modulus (dim.less) | Volume fraction | Surface/ volume ratio | Young's modulus (dim.less) | Volume fraction | Surface/ volume ratio | Young's modulus (dim.less) |
| Initial | 0.148 | 0.258 | 2.186 | 0.146 | 0.211 | 1.748 | 0.143 | 0.164 | 0.989 |
| Optimized | 0.148 | 0.258 | 3.403 | 0.146 | 0.213 | 2.444 | 0.143 | 0.167 | 1.190 |

significant for applications where a high surface-to-volume ratio plays a crucial role. For instance, studies have demonstrated the advantageous use of TPMS structures for bone implants, due to their high surface-to-volume ratio [27]. Another application is the heat exchanger, where a high surface-to-volume ratio is essential for effective heat transfer [28].

The table also shows that the dimensionless effective modulus of elasticity (Young's modulus) changes between the initial and the shape-optimized structure. The volume redistribution led to a visible increase in the effective modulus of elasticity for all structures.

The diamond structure showed an improvement of up to 55 %, the gyroid structure an improvement of up to 40 %, and the primitive structure an improvement of around 20 %. Furthermore, it can be observed that regardless of the optimization, the diamond structure, followed by the gyroid structure, has the highest Young modulus. This order is maintained after optimization, after which the gyroid structure has a higher Young modulus than the non-optimized diamond structure. Wallat et al. [26] describe the layer-wise volume redistribution of the optimized structures in the $y$-direction, compared to the initial structures and the resulting reduction in elastic strain energy in more detail.

This pursues two objectives: the experimental validation of the phase-field-optimized structures and the comparison of the results with those of the simulations. The following sections will explain the manufacture of the structures and the testing procedure. Finally, the results from the experimental setup will be discussed. This work will show that the shape-optimized structures can withstand higher loads on average and that the sequence of experimental data agrees with the simulated results. This knowledge offers new possibilities for the design and application-specific adaptation of complex structures.

## 2. Experimental validation

The experimental validation of the phase-field-based shape optimization will be performed according to the ASTM D1621 standard, "Standard Test Method for Compressive Properties of Rigid Cellular Plastics" [29]. The test specimen dimensions, the test procedure, and the subsequent evaluation of the results are adapted to this standard.

### 2.1. Manufacture of structures

The initial and optimized structures were produced using the stereolithography (SLA) 3D printer *ELEGOO MARS 2*. Quan et al. give a good overview of the difficulties and challenges of photo-curing 3D printing technologies such as SLA [9]. The printing material used was the *Standard Photopolymer Resin* (Elegoo Inc) in white color. The single-cell structures were duplicated with a cell size of 30 mm in the x- and $z$-directions. Each specimen has dimensions of 60 mm×30 mm×60 mm (in the x, y, and z directions). Five samples were tested for each specimen. Fig. 2 illustrates a representative candidate of each type of the printed structures.

The theoretically calculated weight for the printed diamond structure with a density of 1.2 g/cm$^3$, as specified in Table 1, is 19.18 g. Accordingly, the weights of the gyroid and primitive structure are 18.92 g and 18.53 g, respectively. The average values ($\overline{m}$) of the printed samples and their standard deviations ($\tilde{m}$) are listed in Table 2. A breakdown of the weights of individual samples can be found in Appendix Table 6.

Overall, the mean value for each sample deviates from the theoretically calculated sample weight by less than 1 %. As can be seen from the standard deviation, the samples show only minimal variations. It can be observed that the primitive samples show the smallest deviations in both the optimized and non-optimized cases. In contrast, the optimized diamond structure has the highest variation at 0.47 g. One possible reason for these weight fluctuations could be the presence of excess material residues that remained attached to the surface of the samples, despite subsequent acetone treatment. Since the diamond and gyroid structures have the highest surface-to-volume ratios, as shown in Table 1, this could explain why the primitive structure has the least weight variation among the structures.

### 2.2. Mechanical testing and evaluation

For the experiments, the *inspekt 200* machine from *Hegewald & Peschke* is used. The compression is initiated with a pressure of 0.03 kPa, and the testing speed is set to 2.95 mm/min. The test is terminated as soon as approximately 13 % of the original thickness is reached. For subsequent evaluations, the values are zeroed from a force load of 10 N. Fig. 3 uses the example of the diamond structure to illustrate the development of the initial state and the linear-elastic and plastic ranges. At the beginning of the structural collapse, i.e., the failure in the plastic range, the data were truncated for better comparability.

The determination of the effective modulus of elasticity is based on the ASTM D1621 standard. The modulus of elasticity was calculated as follows:

$$E = \frac{W H}{A D}, \tag{1}$$

with the load $W$ [N], the initial specimen height $H$ [m], the initial horizontal cross-sectional area in $A$ [m$^2$], and the deformation $D$ [m]. For the determination of $D$ and $W$, two localized areas of the sample from the linear-elastic range were chosen. However, it should be noted that there are no specific guidelines for the selection of these locations. To determine the value D, the local area of each sample in which the strain is 0.1 % was selected. To obtain a consistent determination of the quantity W, the respective values at which the strain is 30 % of the difference between the strain at 0.1 % and the strain at the maximum stress were considered. Furthermore, it must be emphasized that for the horizontal cross-sectional area in $A$, [m$^2$], the area of the samples was treated as if it were a solid material.

## 3. Results and discussion

The following section compares the simulation-based data with the experimental results, followed by an examination in the plastic regime. Volume conservation during the optimization process ensures that the volume of the initial and optimized structures remains the same, which guarantees a better comparability of the structures. Overall, the experimental validation of the phase-field-based shape-optimized TPMS structures demonstrates that the optimization has improved the linear-elastic range and change in the plastic regime. In Fig. 4, the load–displacement curves are recorded, and for each cell type ("Type = D": Diamond; "Type = G": Gyroid; "Type = P": Primitive), the respective samples have been averaged. Additionally, their standard deviation is shown in the diagram, where the orange line represents the optimized

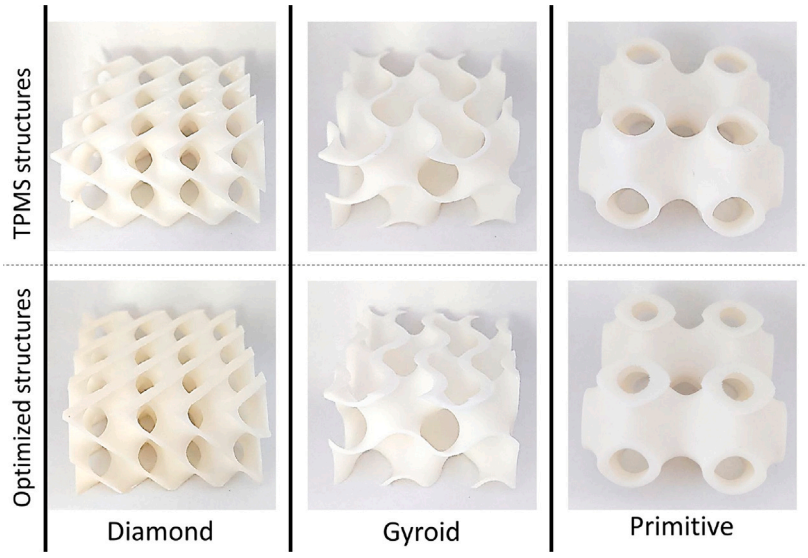


**Fig. 2.** Printed structures: Top: The original TPMS-structures; bottom: The optimized TPMS structures.

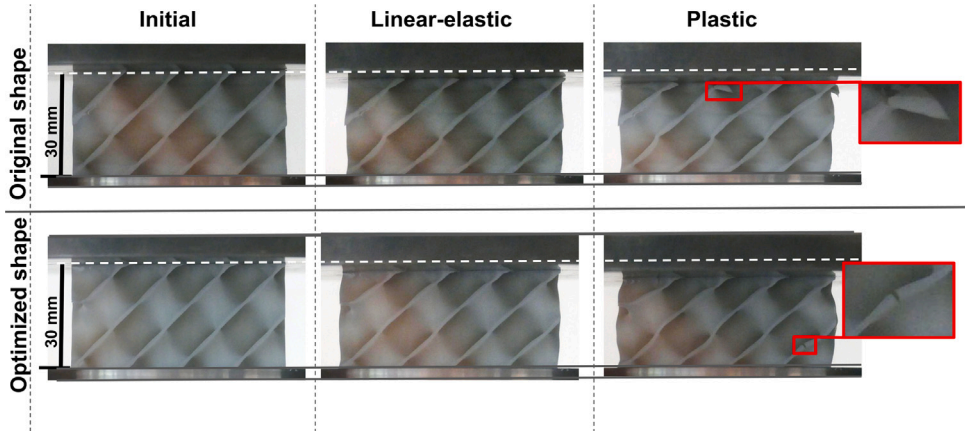


**Fig. 3.** The diamond structure (top) and the shape-optimized diamond structure (bottom): Representation of the initial structure, as well as the structure in the linear-elastic and plastic range during the compression test.

**Table 2**
Average weight ($\bar{m}$) and standard deviation ($\tilde{m}$) of the printed structures.

| | | Diamond | | Gyroid | | Primitive | |
|---|---|---|---|---|---|---|---|
| | | Initial | Optimized | Initial | Optimized | Initial | Optimized |
| $\bar{m}$ | [g] | 19.281 | 19.018 | 18.9178 | 18.8896 | 18.572 | 18.5302 |
| $\tilde{m}$ | [g] | 0.108 | 0.420 | 0.056 | 0.123 | 0.085 | 0.016 |

shape, and the blue line represents the original shape. In the three diagrams, the $y$-axis has the same scaling to allow a comparison between the three structures. It can be seen that the initial diamond structure (blue line, first diagram "Type = D") can absorb the highest load in the load–displacement curve, followed by the gyroid and then the primitive structure. The complete evaluation and interpretation of the results from the diagrams can be found in Section 3.

### 3.1. Validation of the phase-field shape optimization model

Purely linear-elastic behavior cannot be achieved in porous structures [30–33]. However, Fig. 4 clearly visualizes the quasi-elastic range. In [33], CuCrMo structures with gyroid, diamond-shaped and primitive topology and different volume fractions (ranging from 0.2 to 0.4) show elastic behavior at low strain followed by a sudden collapse. The diamond structures exhibit the highest load-bearing capacity, followed by the gyroid structures, and, finally, the primitive structures [33]. Our shape-optimized structures reveal improvements in the linear-elastic and plastic ranges, compared to the original structures. The shape optimization reduces stress concentrations, which leads to a more uniform stress distribution in the component and prevents material failure. For the experiments, the average modulus of elasticity $\bar{E}$ and the standard derivative $\tilde{E}$ can be found in the top two rows of Table 3. These values were determined from the experimental results using Eq. (1), described in Section 2.2. The values for each sample can be obtained from Table 8 in the appendix. When considering the standard deviation, the optimized diamond structures have the highest variance, while the optimized primitive structures have the lowest variance.

With 57.377 %, the optimization of the diamond structure achieves the highest increase in the effective modulus of elasticity in the linear elastic range, followed by the gyroid structure with 23.04 %. For the primitive structure, this increase averages 13.37 %. To establish comparability between the simulation-based dimensionless modulus ($E_{\text{Sim}}$)

**Table 3**
Comparison of the effective modulus of elasticity from the experiments (mean: $\bar{E}$, standard deviation: $\tilde{E}$) and simulations (dimensionless: $E_{\text{Sim}}$, dimensionalized: $E_{\text{SimDim}}$).

| | | Diamond | | Gyroid | | Primitive | |
|---|---|---|---|---|---|---|---|
| | | Initial | Optimized | Initial | Optimized | Initial | Optimized |
| $\bar{E}$ | [MPa] | 33.369 | 52.515 | 27.491 | 33.826 | 14.470 | 16.404 |
| $\tilde{E}$ | [MPa] | 4.664 | 7.142 | 4.753 | 4.881 | 2.531 | 1.710 |
| $E_{\text{Sim}}$ | [–] | 2.186 | 3.403 | 1.748 | 2.444 | 0.989 | 1.190 |
| $E_{\text{SimDim}}$ | [MPa] | 31.314 | 48.748 | 25.040 | 35.010 | 14.164 | 17.047 |

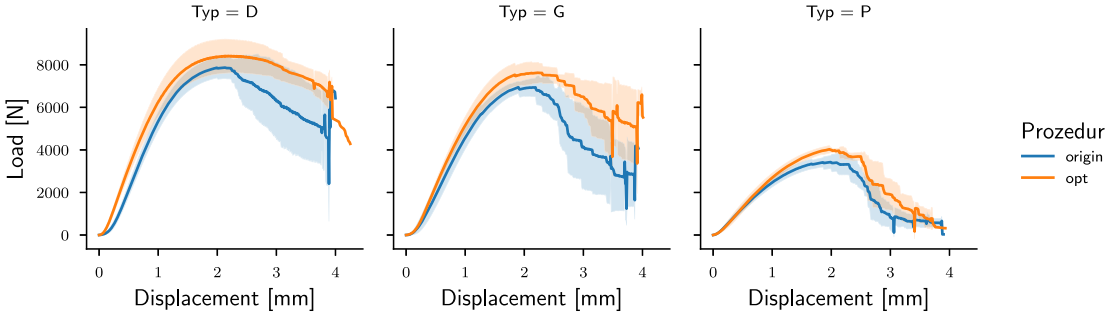


**Fig. 4.** Load–displacement curve: Average values of the compression test for diamond (D), gyroid (G), and primitive (P). (For interpretation of the references to color in this figure legend, the reader is referred to the web version of this article.)

and the experimental data, the dimensionless modulus is converted into a corresponding dimensional modulus $E_{\text{SimDim}}$ [MPa], by calculating the effective unit stress for each sample. The density of the material [$\text{kg}/\text{m}^3$] and the cross-sectional area [$\text{m}^2$] of each sample are physically predetermined. Consequently, the time [s] represents the adjustable characteristic parameter to be determined based on the experimental data. In the present case, the characteristic time is about 0.915 s, which yields a unit stress of 14.32 MPa. The bottom rows of Table 3 compare the dimensionless moduli of elasticity $E_{\text{Sim}}$ and the dimensionalized moduli of elasticity $E_{\text{SimDim}}$ with the average experimental moduli of elasticity for each topology and optimization state.

For better comparability, the determined values of Young's modulus, belonging to the respective samples from the experimental assessment, are presented in a box plot, and the dimensionalized simulated data are marked in red within the respective box plots (see Figs. 5–7). The arithmetic mean of the experimental data is indicated by a black bold cross, while the outliers of the samples are marked by a black circle. It is evident that there is at least one outlier in the experimental data. The whiskers represent the standard deviation from the mean value. The dimensionalized simulated data are represented by a red dashed line in each box plot. The box plots show that the simulated values lie within the standard deviation of the experimental values. In some cases, this value is also within the quartiles and close to the mean value (black cross) of the experimental data. The dimensionalized Young modulus of the optimized diamond structure is farthest from the mean value of the experimental data, while that of the primitive structure is almost the same. The box plots show that scaling establishes a clear correlation between the simulation and the experimental data.

The ability to convert dimensionless data into dimensional data is crucial for future research. It is also important to emphasize that the conversion can be applied even if the simulation data relate to different material properties and cell dimensions (see Section 1 and [26]). This underlines that a load-specific shape optimization of complex cell structures is possible by using dimensionless data with the phase-field method. In the field of linear elasticity, shape optimization leads to a structure that is independent of material properties and dimensions. This can also be confirmed if a different base material is used for the dimensionalization. For example, this investigation considered polylactide (PLA) under equal load conditions. Table 4 lists the simulated effective modulus of PLA which can also be scaled to the experimental

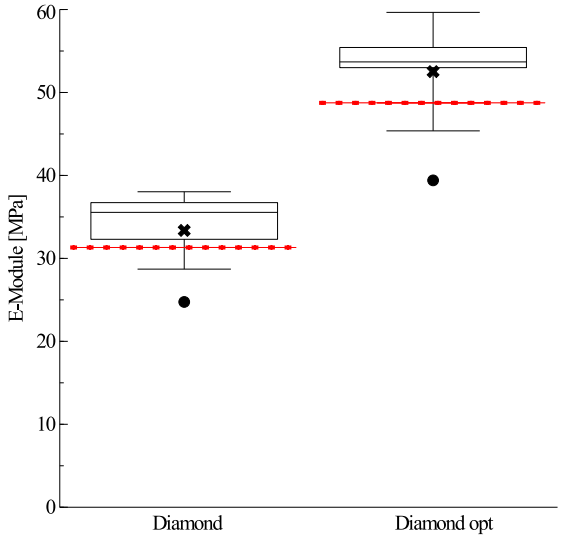


**Fig. 5.** Diamond structure: Comparison of the experimental data with the dimensionalized (red dashed line) simulated data. Representation of the experimental data in a box plot: with upper and lower quantile and median, whereby the standard deviation is marked by the whiskers. The mean value of the experimental data is indicated by a cross and the outliers by circles.

modulus by a constant material-specific factor. Furthermore, a comparison of the two dimensionless parameters (modulus calculated from the aluminum alloy and modulus based on PLA) is also possible. These parameters can be converted into each other, with a factor of 0.1. This indicates that the simulation in this case is independent of the material. This observation is consistent with previous results of 2D studies.

Overall, it is demonstrated that shape optimization in the linear-elastic range is accompanied by an increase in the effective modulus of elasticity (Young's modulus) and, consequently, an increase in stiffness. This result has been presented with convincing agreement in both simulations and experiments.

**Table 4**
Comparison of the originally simulated effective modulus of elasticity ($E_{Sim}$) and the experimentally determined modulus of elasticity ($\bar{E}$) with modified simulative material properties ($E_{Sim\ PLA}$).

| | | Diamond | | Gyroid | | Primitive | |
|---|---|---|---|---|---|---|---|
| | | Initial | Optimized | Initial | Optimized | Initial | Optimized |
| $E_{Sim\ PLA}$ | [MPa] | 0.315 | 0.521 | 0.255 | 0.380 | 0.147 | 0.188 |
| $E_{Sim\ PLA}/E_{Sim}$ | [–] | 0.01 | 0.01 | 0.01 | 0.01 | 0.01 | 0.01 |
| $\bar{E}/E_{Sim\ PLA}$ | [–] | 105.93 | 100.797 | 107.808 | 89.016 | 98.435 | 87.255 |

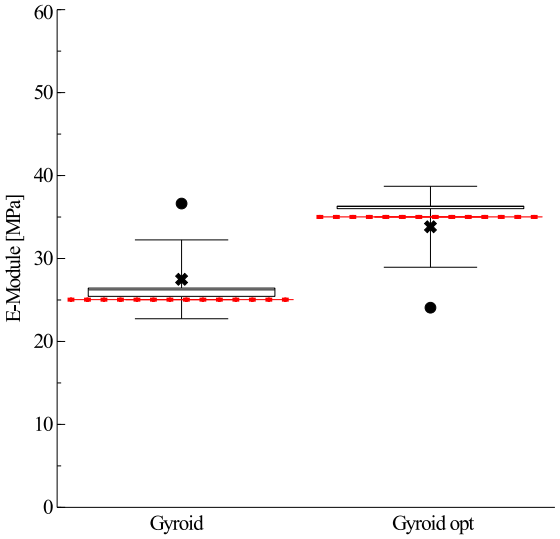


**Fig. 6.** Gyroid structure: Comparison of the experimental data with the dimensionalized (red dashed line) simulated data. Representation of the experimental data in a box plot: with upper and lower quantile and median, whereby the standard deviation is marked by the whiskers. The mean value of the experimental data is indicated by a cross and the outliers by circles.

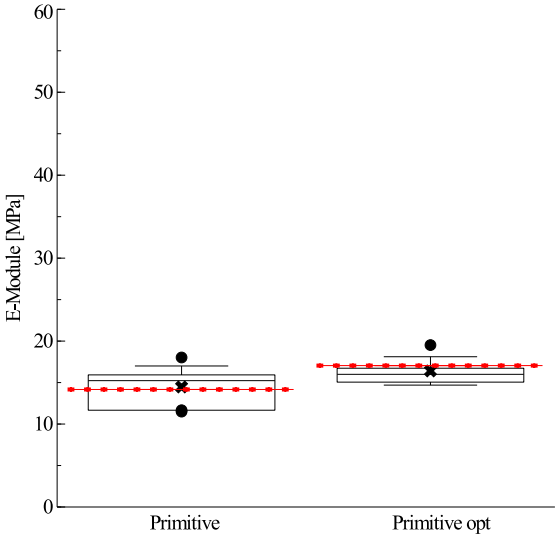


**Fig. 7.** Primitive structure: Comparison of the experimental data with the dimensionalized (red dashed line) simulated data. Representation of the experimental data in a box plot: with upper and lower quantile and median, whereby the standard deviation is marked by the whiskers. The mean value of the experimental data is indicated by a cross and the outliers by circles.

### *3.2. Influence on plastic deformation*

Apart from the linear-elastic range, the plastic range is considered. In addition to the increase in the effective elastic modulus of elasticity, a change in the plastic deformation range can be observed. This aspect becomes apparent from the analysis of the load–displacement curves (Fig. 4) and the average maximum stress values ($\mu_{stress}[MPa]$) in Table 5. An increase in the effective modulus of elasticity consequently leads to a shift in the plastic deformation range.

It can be observed that the optimization of the primitive structure in the linear-elastic range has the greatest effect on the maximum stress by about 16.40 %, despite the smallest increase in the effective modulus of elasticity by 13.37 %. While the increase in the effective modulus of elasticity has a direct effect on the overall stiffness of the structures, changes in the maximum stress can be attributed to the volume redistribution during the shape optimization process. Similar to the standard deviation of the effective Young modulus from Table 3, the standard deviation of the maximum stress has the highest value for the diamond structure, while the standard deviation of the optimized primitive structure shows the lowest variation between the samples. Furthermore, the individual shape-optimized structures exhibit fewer sudden failure patterns than the non-optimized structures. In conjunction with the shift in the plastic deformation range, this results in a higher energy absorption capacity of the optimized structure, making it more suitable for additional applications such as crash structures. The improved mechanical performance of the optimized structures makes them particularly promising for deployment in various engineering applications where energy absorption and resistance to plastic deformation are crucial factors. The values for each pattern can be found in Table 7 in the appendix.

## 4. Conclusion and outlook

This paper has focused on the experimental validation of load-specific shape-optimized TPMS unit cells. In previous work, TPMS unit cells were shape optimized under unilateral compression, integrating a novel phase field method with a shape optimization scheme. The present experimental validation shows a correlation between the simulation and the experimental data. To achieve this, the original and optimized individual TPMS unit cell structures were replicated in the x- and $z$-directions and manufactured using SLA 3D printing. Compression tests showed that the simulation results agree well with the order of magnitude of the experimental data. As a result, shape optimization leads to an increase in the effective modulus of elasticity, on average, compared to the original structure. For better comparability, the dimensionless data were scaled between simulation-based dimensionless data and the experimental data. This scaling leads to an agreement between the simulated scaled effective modulus and the calculated modulus, with a maximum deviation of 6 %. Furthermore, it is discussed that optimization in the linear elastic regime shifts the plastic range. Despite the smallest increase in the effective modulus of elasticity, observed when optimizing the primitive structure, this type of structure exhibits the highest percentage increase in maximum stress. In addition, the load–displacement curves illustrate that the shape-optimized structures collapse less abruptly, which leads to a longer plateau in the plastic range and thus to a greater energy absorption capacity. In summary, the comparison between experimental and simulated data confirms that the computational shape optimization based on a phase-field approach is a valuable and reliable tool for optimizing the morphology of porous structures under mechanical loading. This provides a resource-efficient method for virtual material design with a

**Table 5**
Average maximum stress ($\bar{\sigma}_{max}$) and standard deviation ($\tilde{\sigma}_{max}$) of TPMS structures in MPa.

| | | Diamond | | Gyroid | | Primitive | |
|---|---|---|---|---|---|---|---|
| | | Initial | Optimized | Initial | Optimized | Initial | Optimized |
| $\bar{\sigma}_{max}$ | [MPa] | 12.732 | 13.488 | 11.38 | 12.326 | 5.636 | 6.558 |
| $\tilde{\sigma}_{max}$ | [MPa] | 0.779 | 1.264 | 0.492 | 0.846 | 0.412 | 0.226 |

versatile and extensive application potential. Despite the use of dimensionless data for the simulation with different material parameters and structure sizes, the subsequent scaling reveals a correlation between the experimental and simulation-based data. The use of dimensionless data in a single-phase material simulation leads to a material- and dimension-independent load-specific shape optimization, while maintaining the volume. These results underline the potential of the phase field method as a promising tool for the load-specific optimization of complex porous structures. The optimization of multicellular structures or under different load conditions is also possible. This novel design approach is important in various fields, such as bone scaffold design, where shape optimization maintains a high surface-to-volume ratio and a curved surface that is favorable for bone growth, while introducing load-specific gradients that improve mechanical properties. Furthermore, various studies have already demonstrated that TPMS (based) structures show promise for crash applications [31,34]. For instance, in [34], it was shown that the TPMS-based structures investigated there exhibit higher energy absorption capacity, leading to increased crash safety. Similarly, in the case of the shape-optimized structures studied here, the plastic plateau has been extended, resulting in higher energy absorption capacity of the structures. For this reason, these structures could be suggested for areas of application in which a high impact load occurs and material is to be used sparingly.

At this point, it should be emphasized that tests have been conducted only on a total of six different structures (3 original structures and 3 shape-optimized structures). A correlation with the simulated data could be established for all structures. The presented study can be expanded to other porous structures in order to experimentally validate digitally determined shape optimizations as a result of the phase field method in a similar procedure. In future research work will investigate whether the results of the determined mean values can also be transferred to other sample size of the respective structure type and show the same behavior. In addition, further investigations into phase-field-based topology optimization are a future complementary research direction. In addition, the optimization of the shape and topology of porous structures with reduced volume fractions would be important for lightweight construction applications. Furthermore, the shape optimization of structures under different load conditions, the extension to multiphase materials, and manufacturing restrictions are topics for future research work.

## CRediT authorship contribution statement

**Leonie Wallat:** Writing – original draft, Methodology, Conceptualization. **Arnd Koeppe:** Writing – review & editing. **Michael Selzer:** Writing – review & editing, Supervision. **Marcus Seiler:** Project administration. **Frank Poehler:** Writing – review & editing, Supervision. **Britta Nestler:** Writing – review & editing, Supervision.

## Declaration of competing interest

The authors declare that they have no known competing financial interests or personal relationships that could have appeared to influence the work reported in this paper.

## Data availability

Data will be made available on request.

## Acknowledgments

The authors would like to thank Leon Geisen for his editorial support, as well as Mrs. Kirchlechner and Prof. Dr.-Ing. Uwe Wasmuth for their assistance with the mechanical testing of the structures. Thanks also go to the German Federal Ministry of Economics and Climate Protection, which is funding the ZIM projects KK5134113SK1 and KK5446701SK1. Furthermore, funding within the programs MSE and KNMF, No. 43.31.01, provided by the Helmholtz Association, Germany is gratefully acknowledged.

## References

[1] K. Mu, A. Kueh, P. Shek, Hydroelastic responses of plates with sinusoidal tubercles under perpendicularly loaded flow, Ocean Eng. 219 (2021) 108301, http://dx.doi.org/10.1016/j.oceaneng.2020.108301, URL https://www.sciencedirect.com/science/article/pii/S0029801820312166.

[2] J. Berger, H. Wadley, R. McMeeking, Mechanical metamaterials at the theoretical limit of isotropic elastic stiffness, Nature 543 (2017) http://dx.doi.org/10.1038/nature21075.

[3] L.J. Gibson, Cellular solids, MRS Bull. 28 (4) (2003) 270–274, http://dx.doi.org/10.1557/mrs2003.79.

[4] J. Shi, L. Zhu, L. Li, Z. Li, J. Yang, X. Wang, A TPMS-based method for modeling porous scaffolds for bionic bone tissue engineering, Sci. Rep. 8 (2018) http://dx.doi.org/10.1038/s41598-018-25750-9.

[5] A.H. Foroughi, M.J. Razavi, Shape optimization of orthopedic porous scaffolds to enhance mechanical performance, J. Mech. Behav. Biomed. Mater. 128 (2022) 105098, http://dx.doi.org/10.1016/j.jmbbm.2022.105098, URL https://www.sciencedirect.com/science/article/pii/S175161612200025X.

[6] M. Rezapourian, I. Jasiuk, M. Saarna, I. Hussainova, Selective laser melted Ti6Al4V split-P TPMS lattices for bone tissue engineering, Int. J. Mech. Sci. 251 (2023) 108353, http://dx.doi.org/10.1016/j.ijmecsci.2023.108353, URL https://www.sciencedirect.com/science/article/pii/S0020740323002552.

[7] D.-J. Yoo, Advanced porous scaffold design using multi-void triply periodic minimal surface models with High Surface Area to volume ratios, Int. J. Precis. Eng. Manuf. 15 (2014) 1657–1666, http://dx.doi.org/10.1007/s12541-014-0516-5.

[8] O. Alketan, R. Abu Al-Rub, Multifunctional mechanical-metamaterials based on triply periodic minimal surface lattices: A review, Adv. Eng. Mater. (2019) http://dx.doi.org/10.1002/adem.201900524.

[9] H. Quan, T. Zhang, H. Xu, S. Luo, J. Nie, X. Zhu, Photo-curing 3D printing technique and its challenges, Bioact. Mater. 5 (1) (2020) 110–115, http://dx.doi.org/10.1016/j.bioactmat.2019.12.003, URL https://www.sciencedirect.com/science/article/pii/S2452199X19300714.

[10] L. Wallat, P. Altschuh, M. Reder, B. Nestler, F. Poehler, Computational design and characterisation of gyroid structures with different gradient functions for porosity adjustment, Materials 15 (10) (2022) 3730, http://dx.doi.org/10.3390/ma15103730, URL http://dx.doi.org/10.3390/ma15103730.

[11] D. Li, W. Liao, N. Dai, Y.M. Xie, Comparison of mechanical properties and energy absorption of sheet-based and strut-based gyroid cellular structures with graded densities, Materials 12 (13) (2019) 2183, http://dx.doi.org/10.3390/ma12132183, URL http://dx.doi.org/10.3390/ma12132183.

[12] F. Liu, Z. Mao, P. Zhang, D.Z. Zhang, J. Jiang, Z. Ma, Functionally graded porous scaffolds in multiple patterns: New design method, physical and mechanical properties, Mater. Des. 160 (2018) 849–860, http://dx.doi.org/10.1016/j.matdes.2018.09.053, URL https://www.sciencedirect.com/science/article/pii/S026412751830755X.

[13] S.Y. Choy, C.-N. Sun, K.F. Leong, J. Wei, Compressive properties of functionally graded lattice structures manufactured by selective laser melting, Mater. Des. 131 (2017) 112–120, http://dx.doi.org/10.1016/j.matdes.2017.06.006, URL https://www.sciencedirect.com/science/article/pii/S0264127517305890.

[14] J. Plocher, A. Panesar, Effect of density and unit cell size grading on the stiffness and energy absorption of short fibre-reinforced functionally graded lattice structures, Addit. Manuf. 33 (2020) 101171, http://dx.doi.org/10.1016/j.addma.2020.101171, URL https://www.sciencedirect.com/science/article/pii/S2214860420305431.

[15] Q. Yu, Q. Xia, Y. Li, A phase field-based systematic multiscale topology optimization method for porous structures design, J. Comput. Phys. 466 (2022) 111383, http://dx.doi.org/10.1016/j.jcp.2022.111383, URL https://www.sciencedirect.com/science/article/pii/S0021999122004454.

[16] Y. Zheng, Z. Luo, Y. Wang, Z. Li, J. Qu, C. Zhang, Optimized high thermal insulation by the topological design of hierarchical structures, Int. J. Heat Mass Transfer 186 (2022) 122448, http://dx.doi.org/10.1016/j.ijheatmasstransfer.2021.122448, URL https://www.sciencedirect.com/science/article/pii/S0017931021015465.

[17] F. Li, X. Hu, A phase-field method for shape optimization of incompressible flows, Comput. Math. Appl. 77 (4) (2019) 1029–1041, http://dx.doi.org/10.1016/j.camwa.2018.10.029, URL https://www.sciencedirect.com/science/article/pii/S0898122118306266.

[18] K. Mu, A. Kueh, P. Shek, M.M. Haniffah, B. Tan, Flow responses alteration by geometrical effects of tubercles on plates under the maximal angle of attack, Proc. Inst. Mech. Eng. C 235 (19) (2021) 3975–3987, http://dx.doi.org/10.1177/0954406220975434.

[19] L. Blank, H. Garcke, L. Sarbu, T. Srisupattarawanit, V. Styles, A. Voigt, Phase-field approaches to structural topology optimization, in: Constrained Optimization and Optimal Control for Partial Differential Equations, Vol. 160, 2012, http://dx.doi.org/10.1007/978-3-0348-0133-1_13.

[20] T. Takaki, J. Kato, Phase-field topology optimization model that removes the curvature effects, Mech. Eng. J. 4 (2) (2017) 16–00462–16–00462, http://dx.doi.org/10.1299/mej.16-00462.

[21] S. Pech, M. Lukacevic, J. Füssl, Validation of a hybrid multi-phase field model for fracture of wood, Eng. Fract. Mech. 275 (2022) 108819, http://dx.doi.org/10.1016/j.engfracmech.2022.108819, URL https://www.sciencedirect.com/science/article/pii/S0013794422005379.

[22] A. Zhiliakov, Y. Wang, A. Quaini, M. Olshanskii, S. Majd, Experimental validation of a phase-field model to predict coarsening dynamics of lipid domains in multi-component membranes, Biochimica et Biophysica Acta (BBA) - Biomembranes 1863 (1) (2021) 183446, http://dx.doi.org/10.1016/j.bbamem.2020.183446, URL https://www.sciencedirect.com/science/article/pii/S0005273620302893.

[23] K. Pham, K. Ravi-Chandar, C. Landis, Experimental validation of a phase-field model for fracture, Int. J. Fract. 205 (2017) http://dx.doi.org/10.1007/s10704-017-0185-3.

[24] L. Blank, H. Garcke, C. Hecht, C. Rupprecht, Sharp interface limit for a phase field model in structural optimization, SIAM J. Control Optim. 54 (3) (2016) 1558–1584, http://dx.doi.org/10.1137/140989066.

[25] H. Garcke, M. Hinze, C. Kahle, K. Lam, A phase field approach to shape optimization in Navier–Stokes flow with integral state constraint, Adv. Comput. Math. 44 (2018) http://dx.doi.org/10.1007/s10444-018-9586-8.

[26] L. Wallat, M. Reder, M. Selzer, F. Poehler, B. Nestler, Shape optimization of porous structures by phase-field modelling with strain energy density reduction, Mater. Today Commun. (2023) 107018, http://dx.doi.org/10.1016/j.mtcomm.2023.107018, URL https://www.sciencedirect.com/science/article/pii/S2352492823017099.

[27] E. Maevskaia, J. Guerrero, C. Ghayor, I. Bhattacharya, F.E. Weber, Triply periodic minimal surface-based scaffolds for bone tissue engineering: A mechanical, in vitro and in vivo study, Tissue Eng. A 29 (19–20) (2023) 507–517, http://dx.doi.org/10.1089/ten.tea.2023.0033, PMID: 37212290.

[28] T. Dixit, E. Al-Hajri, M.C. Paul, P. Nithiarasu, S. Kumar, High performance, microarchitected, compact heat exchanger enabled by 3D printing, Appl. Therm. Eng. 210 (2022) 118339, http://dx.doi.org/10.1016/j.applthermaleng.2022.118339, URL https://www.sciencedirect.com/science/article/pii/S1359431122002976.

[29] Standard test method for compressive properties of rigid cellular plastics, 2000, 1621 – 00.

[30] K. Nelson, C.N. Kelly, K. Gall, Effect of stress state on the mechanical behavior of 3D printed porous Ti6Al4V scaffolds produced by laser powder bed fusion, Mater. Sci. Eng. B 286 (2022) 116013, http://dx.doi.org/10.1016/j.mseb.2022.116013, URL https://www.sciencedirect.com/science/article/pii/S0921510722004019.

[31] L. Wallat, M. Selzer, U. Wasmuth, F. Poehler, B. Nestler, Energy absorption capability of graded and non-graded sheet-based gyroid structures fabricated by microcast processing, J. Mater. Res. Technol. 21 (2022) 1798–1810, http://dx.doi.org/10.1016/j.jmrt.2022.09.093, URL https://www.sciencedirect.com/science/article/pii/S2238785422015009.

[32] D. Qin, L. Sang, Z. Zhang, S. Lai, Y. Zhao, Compression performance and deformation behavior of 3D-printed PLA-based lattice structures, Polymers 14 (5) (2022) http://dx.doi.org/10.3390/polym14051062, URL https://www.mdpi.com/2073-4360/14/5/1062.

[33] O. Gülcan, U. Simsek, O. Cokgunlu, M. Özdemir, P. Şendur, G.G. Yapici, Effect of build parameters on the compressive behavior of additive manufactured CoCrMo lattice parts based on experimental design, Metals 12 (7) (2022) URL https://www.mdpi.com/2075-4701/12/7/1104.

[34] H. Wang, D. Tan, Z. Liu, H. Yin, G. Wen, On crashworthiness of novel porous structure based on composite TPMS structures, Eng. Struct. 252 (2022) 113640, http://dx.doi.org/10.1016/j.engstruct.2021.113640, URL https://www.sciencedirect.com/science/article/pii/S0141029621017296.